SANDIA REPORT
SAND2020-4327
Printed Click to enter a date

Sandia National Laboratories

Near-Field Imaging of Shallow Chemical Explosions in Granite Using Change Detection Methods with Surface and Borehole Seismic Data

Charles R. Hoots, Robert E. Abbott, Leiph Preston, Hunter A. Knox, and Paul C. Schwering

Prepared by
Sandia National Laboratories
Albuquerque, New Mexico
87185 and Livermore,
California 94550

Issued by Sandia National Laboratories, operated for the United States Department of Energy by National Technology & Engineering Solutions of Sandia, LLC.

Available to DOE and DOE contractors from
U.S. Department of Energy
Office of Scientific and Technical Information
P.O. Box 62
Oak Ridge, TN 37831

Telephone: (865) 576-8401
Facsimile: (865) 576-5728
E-Mail: reports@osti.gov
Online ordering: http://www.osti.gov/scitech

Available to the public from
U.S. Department of Commerce
National Technical Information Service
5301 Shawnee Rd
Alexandria, VA 22312

Telephone: (800) 553-6847
Facsimile: (703) 605-6900
E-Mail: orders@ntis.gov
Online order: https://classic.ntis.gov/help/order-methods/

ABSTRACT

Explosions detonated in geologic media damage it in various ways via processes that include vaporization, fracturing, crushing of interstitial pores, etc. Seismic waves interact with the altered media in ways that could be important to the discrimination, characterization, and location of the explosions. As part of the Source Physics Experiment, we acquired multiple pre- and post-explosion near-field seismic datasets and analyzed changes to seismic P-wave velocity. Our results indicate that the first explosion detonated in an intact media can cause fracturing and, consequently, a decrease in P-wave velocity. After the first explosion, subsequent detonations in the pre-damaged media have limited discernible effects. We hypothesize this is due to the stress-relief provided by a now pre-existing network of fractures into which gasses produced by the explosion migrate. We also see an overall increase in velocity of the damaged region over time, either due to a slow healing process or closing of the fractures by subsequent explosions.

ACKNOWLEDGEMENTS

The authors thank Dan Herold, Bob White, Kale McLin, Ryan Emmit, Maggie Townsend, Curtis Obi, Fred Helsel, Rebekah Lee, Liam Toney, James Knox, Matt Geuss, Nedra Bonal, and Josh Feldman for their direct and invaluable contributions to this work. We also thank Oleg Vorobiev for helpful conversations. We also thank Brian Young for his diligent work in the peer review process.

CONTENTS

LIST OF FIGURES

ACRONYMS AND DEFINITIONS

Abbreviation	Definition
CCC	normalized cross-correlation coefficient
NNSS	Nevada National Security Site
SPE	Source Physics Experiment
SNR	signal-to-noise ratio
AWD	accelerated weight-drop seismic source
GZ	ground zero (surface location of the explosives-containing borehole)
EMP	electromagnetic pulse
DOB	depth of burial
SDOB	scaled depth of burial
TNT	trinitrotoluene
TNT-equivalence	1 kiloton TNT = 4.184×10^{12} Joules
$m / kt^{1/3}$	scaled depth of burial (meters per cube-root kiloton of TNT-equivalent energy)
T_0	apparent first-arrival time of the P-wave
m/s	meters per second (velocity)
P-wave	seismic wave with particle motion polarized along the direction of travel
Hz	Hertz (frequency, cycles per second)
kV	kilovolts

This page left blank

1. INTRODUCTION

Explosions in the subsurface can damage and modify the geologic media in which it is detonated. These effects may be seen through a variety of phenomena, including increased fracturing, evidence of slip on joints, or changes in density or porosity. Effects close to, but not coincident with, the detonation point (such as surface spall and resultant "slapdown") cause damage and can act as secondary seismic sources, separated both temporally and spatially from the explosion (Patton, 1988). The combined effect of damage and spall complicate the seismic source-time function of an ostensibly simple isotropic explosion. The resultant seismic waves, when recorded at a distant site, can show the effects of this damage in frequency content, amplitude, and/or phase (Taylor and Randall, 1989). These phenomena can be difficult to analyze as the source–receiver distance increases, as is the case in nuclear explosion monitoring.

In part to understand these source region effects, the Source Physics Experiment (SPE) program was established to conduct a series of chemical explosions at the Nevada National Security Site (NNSS) (Snelson et al., 2013). During SPE, two series (hereafter referred to as "phases") of chemical explosions were detonated downhole in different geologies. These explosions were well-instrumented with seismo-acoustic sensors at ranges from tens of meters to hundreds of kilometers. The recordings were used as ground truth for improving explosion-source physics modeling codes. SPE Phase I was conducted in granitic geology, and two satellite boreholes, coplanar with the explosives hole for six explosions in total, were installed in order to monitor changes in groundwater level. These satellite holes presented an ideal geometry to conduct cross-borehole seismic studies as the SPE explosions were conducted. This report details the results of multiple before-and-after cross-borehole seismic experiments at the SPE Phase I site.

2. BACKGROUND

SPE Phase I consisted of six chemical explosions conducted in a single 0.9 m diameter borehole at the NNSS (Fig. 1, Snelson et al., 2013). The explosions ranged from 31 to 87 m depth-of-burial and 90 to 5,005 kg TNT-equivalent yield (Fig. 2, red boxes). The detonation medium was the Climax Stock, a Mesozoic granodiorite intrusive body, in Area 15 at the NNSS (Townsend et al., 2012).

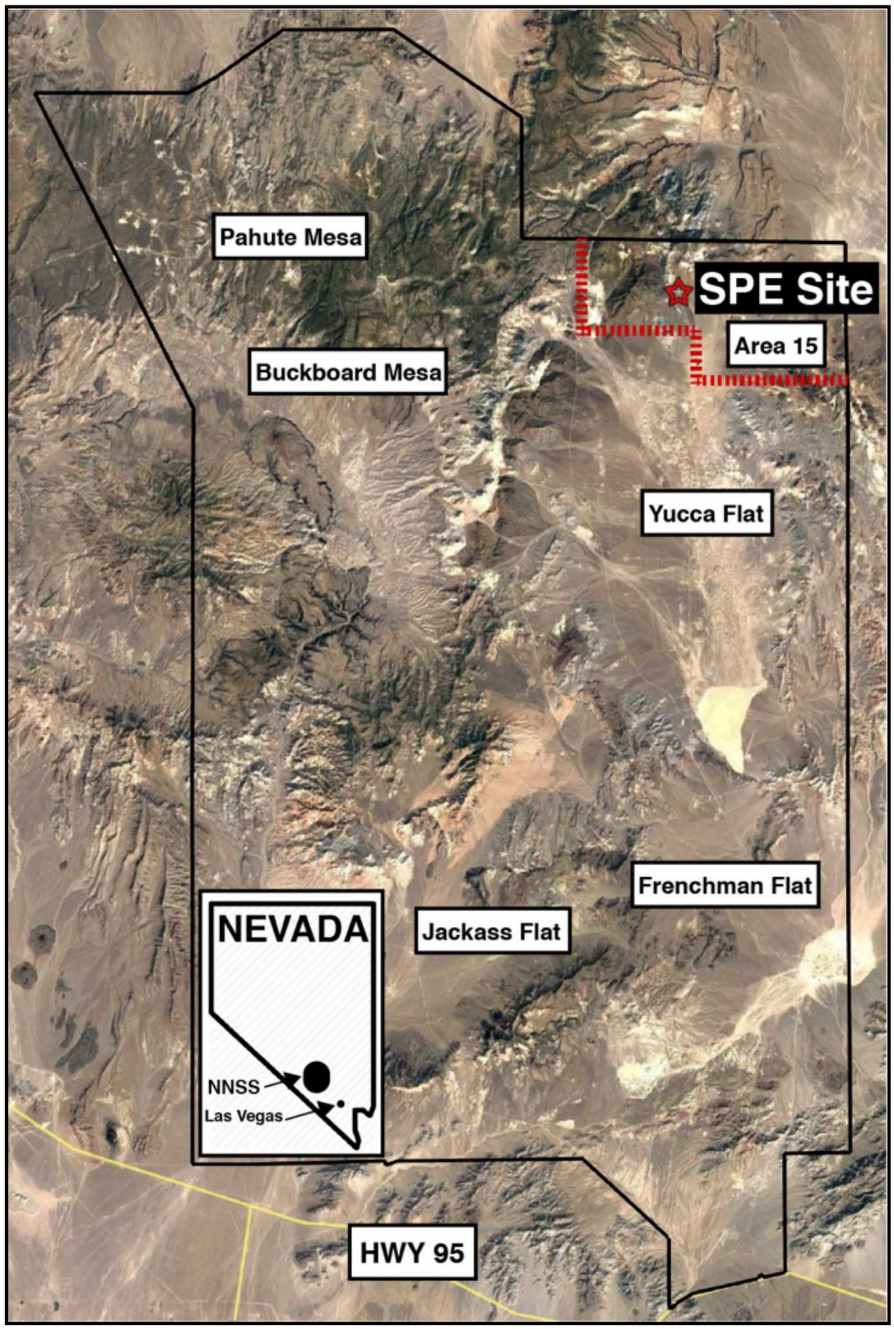

Figure 1. Nevada National Security Site and SPE Site.

Prior to the drilling of ground zero (GZ) we conducted a hammer-and-plate seismic refraction survey to determine the thickness of the weathered zone. This survey revealed P-wave velocity values of approximately 1,200 m/s at the surface, increasing to over 5,000 m/s at 75 m depth (Fig. 3). The surface results indicate that the velocity structure can be modeled as a gradient over a half-space. We interpret the depth of the bottom of the weathered zone to be approximately 25 m.

Unexpectedly, drilling GZ revealed that the test bed was in a region with a perched water aquifer. In order to track water levels over the course of the experiments, four boreholes were drilled, with approximately equal azimuthal distribution, at distances from GZ ranging from 28 m to 48 m. All

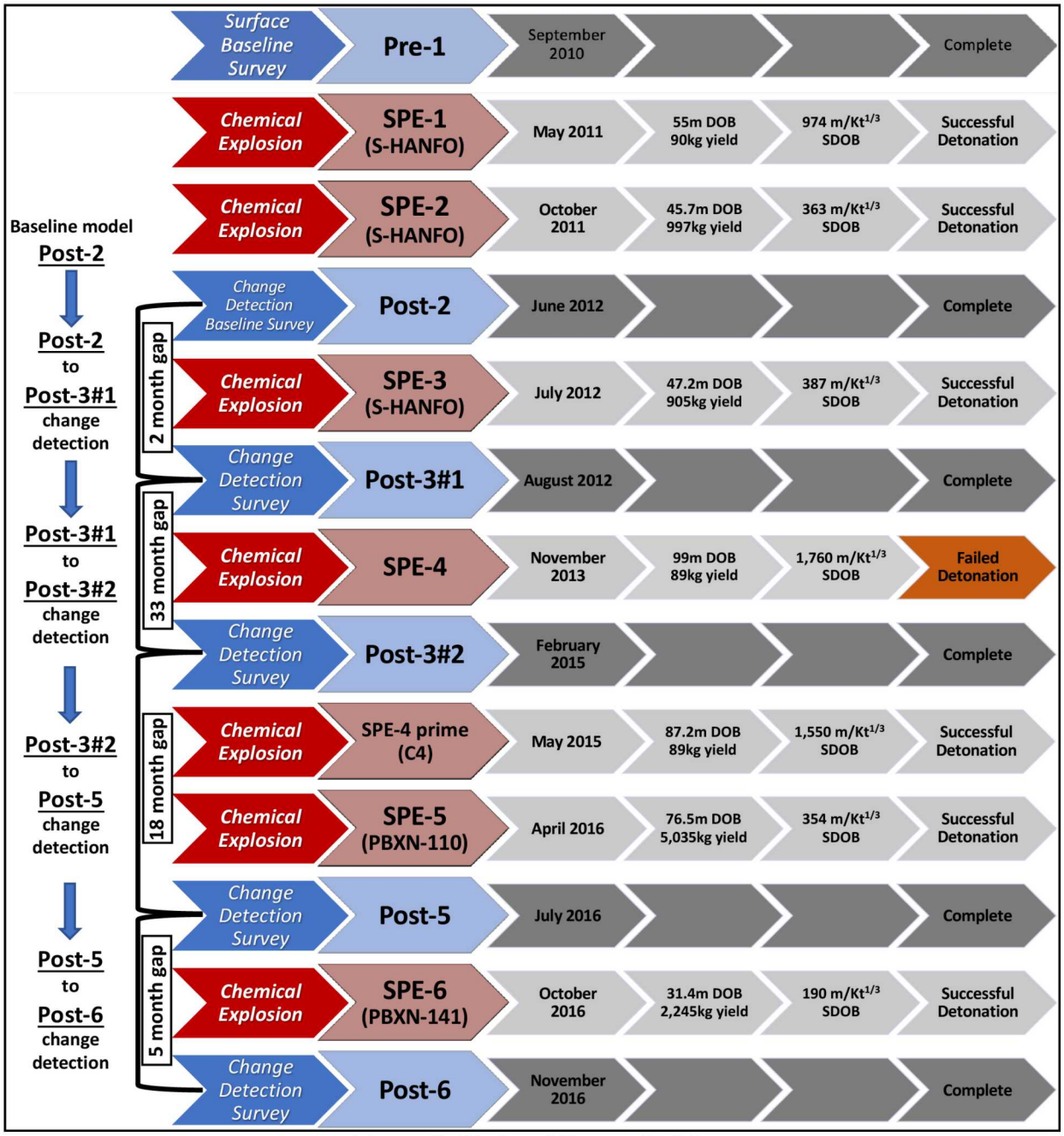

Figure 2. Shot and Survey Matrix.

four boreholes were drilled to be coplanar (two different sets) with GZ so as to be favorable with cross-borehole seismic experiments. Each of the boreholes are 31 cm in diameter, 79 m deep, and uncased. One borehole collapsed at an intermediate depth before a full seismic survey could be conducted, so all results presented here are from the plane including GZ and boreholes BH-009 and BH-189 (Fig. 4).

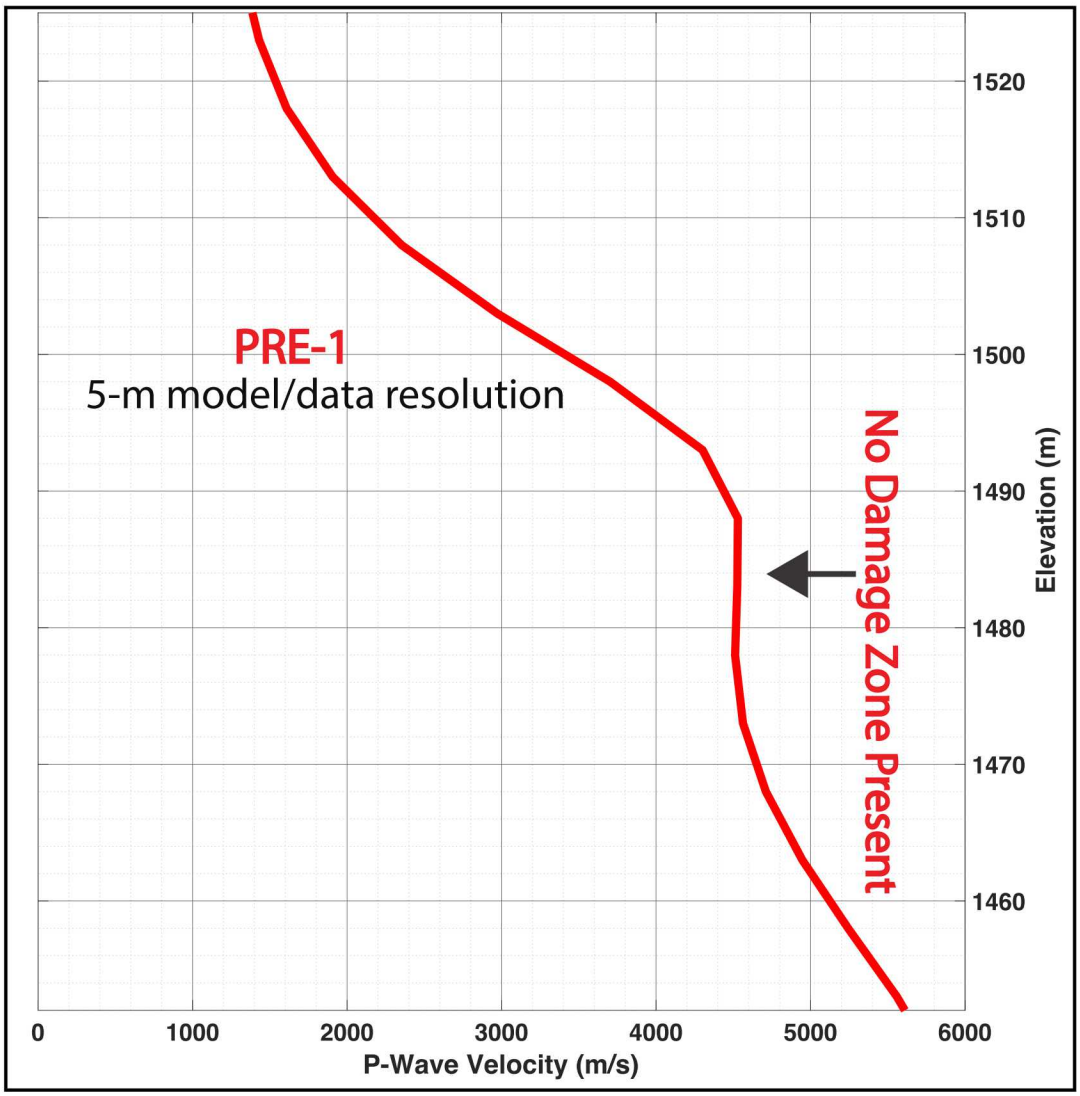

Figure 3. 1D P-wave velocity before the SPE-1 chemical explosion.

3. SURVEY GEOMETRY

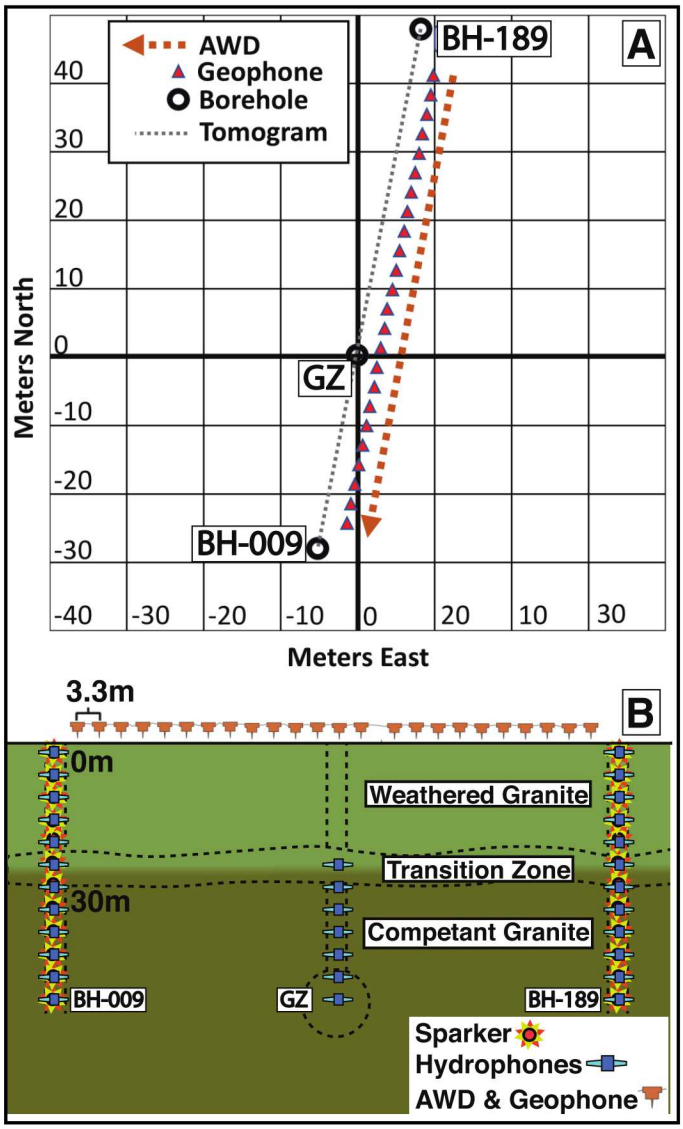

Figure 4. Survey Geometry. 5A is map view, 5B is plan view.

For each seismic campaign, data were collected in and between boreholes BH-009 and BH-189, coplanar with the explosives-emplacement borehole at GZ (Fig. 4). A Geotomographie IPG5000 plasma seismic source (a.k.a. "sparker") and a 24-channel string of hydrophones were utilized in the two monitoring boreholes and GZ (Fig. 4). The inclusion of hydrophones in the GZ borehole in the seismic surveys was determined by the borehole's accessibility, which was dependent on drilling schedule and whether or not the stemming from the previous explosion had been removed. Hydrophones were placed in GZ for the Post-2, Post-3#2, and Post-5 surveys. Sparker shots and hydrophone receivers were both spaced at 1 m depth intervals. Since the sparker source and the hydrophone receivers both need to be submerged in water to operate, BH-009 and BG-189 were filled with water up to the surface. This allowed for deployment of sensors below 1 m depth. However, no water was added to the GZ hole, so sensors could only be installed to the natural water level at the time. This surface of the water table varied but was generally in the vicinity of 15–20 m below the ground surface.

We also used surface sources and surface receivers for each survey. The surface-to-surface component of the survey consisted of an accelerated weight drop (AWD) recorded by twenty-four 3 Hz geophones spanning the two boreholes with 3.3 m spacing (Fig. 4).

4. METHODOLOGY

Examination of the unstacked cross-borehole seismic traces revealed anomalous timing of first-arrivals from within source gathers for the sparker (Fig. 5a, 5b). The AWD records did not suffer from this phenomenon. Without correction for these timing anomalies, stacking the sparker records result in broader first-arrival waveforms with lower SNR (Fig. 5c).

After some analysis, we believe that timing errors were caused by improper triggering of the data recorder. We traced this errant triggering to an electromagnetic pulse (EMP) generated by the rapid discharge of 5 kV of electrical potential that powers the Geotomographie sparker source. We believe that the EMP, which is generated downhole, propagates through the earth and couples with poorly shielded and/or poorly grounded cable systems between the hydrophones and data loggers. The EMP induces a current in the cables which is picked up and interpreted by the system as a triggering signal. This signal is also picked up on string of hydrophones and, because the EMP travels at the speed of light, is visible as a high-frequency pulse arriving simultaneously on all 24 channels well before the arrival of any seismic energy. This property of the EMP means that, in effect, it acts as a fiduciary for T_0 on a set of unstacked traces. By aligning these pulses prior to stacking (Fig. 5d), we are able to correct the timing errors that would have otherwise resulted in lower SNR, degraded stack quality, and erroneous first-arrival times in the stacked traces (Fig. 5e). This correction process will be described in detail below.

4.1. T_0 Alignment

All data were bandpass filtered between 200 Hz and 500 Hz prior to correcting timing statics. The low-cut is for removing standing tube waves in the borehole which are approximately twice the frequency of the normal mode of a ~80 m borehole within a hard rock medium with mean velocity around 6,000 m/s (Houston, 1992). The high-cut filter preserves the EMP as close to a delta function as possible.

We first identify the record from a single shot location with the shortest time difference between the first sample and the EMP first-arrival. This record has the greatest likelihood of all common-source records of having accurate timing. The remaining records for this source location will be aligned to this reference record via cross-correlation of a short time window centered on the EMP. All shots

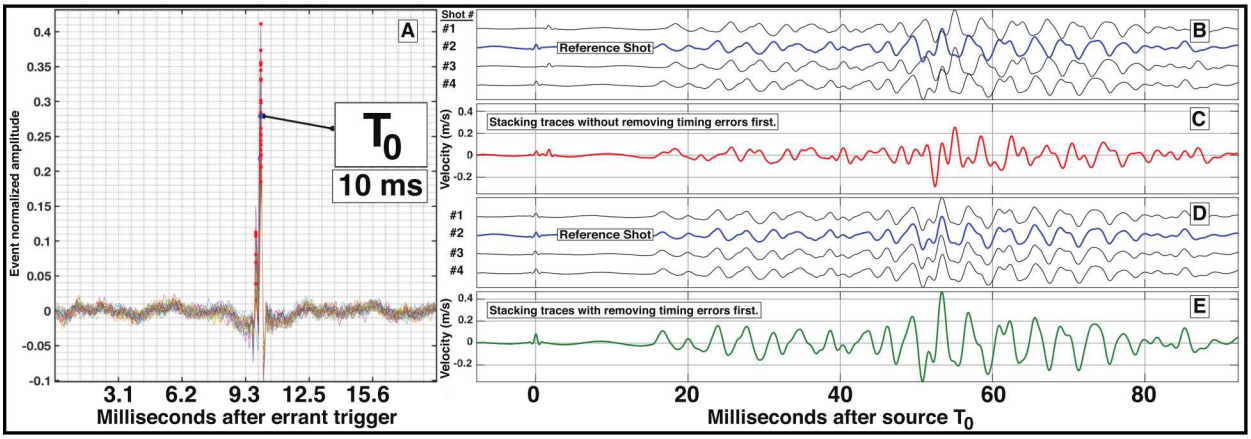

Figure 5. (A) Superposition of 5 different sparker sources on one channel, showing slight misalignment of EMP pulse. (B) EMP pulse and first seismic arrival misaligned on 5 sparker sources. (C) Result of stacking 5 sparker sources without aligning t common time base. (D) EMP pulse and first seismic arrival after correcting misalignment. (E) Result of stacking 5 sparker sources after correcting misalignment.

were upsampled by a factor of ten to provide the potential for sub-sample accuracy in the cross-correlation. Only cross-correlations with a normalized cross-correlation coefficient (CCC) of greater than 0.9 were allowed. All 24 channels of data were correlated with their counterparts on the reference shot. This reduced the potential for error if the EMP, on an individual channel, had small differences from the reference EMP (e.g. subsurface conductivity heterogeneity). Each of the shots were realigned before stacking by the mean of the time lags of all 24 channels (excluding outliers in CCC or time lag).

As can be seen in Fig. 5c, stacking of misaligned records resulted in poor SNR and first-arrival precision. In some cases, the impulsiveness of the first-arriving energy was significantly reduced, which can have adverse consequences when picking phases in a high-velocity, short-offset geometry. By systematically identifying timing errors in pre-stack data and then aligning them, SNR and confidence of the stacked records was improved (Fig. 5e).

4.2. First Break Picking

First-arriving P-waves were picked once the traces were properly aligned and stacked. Early tests illustrated the AWD source coupled poorly into the hydrophones, resulting in very low signal-to-noise ratios (SNR) at the downhole hydrophones. For this reason, we do not use any AWD-to-hydrophone, and likewise, sparker-to-geophone data in the inversions.

For the first cross-borehole experiment (Post-2), traces were picked by hand for both AWD and sparker sources. Subsequent experiments featured hand-picking for AWD sources only. Sparker sources were automatically picked using a modified version of the same process used to align the records in the previous step. In this case, the hand-picked arrivals for Post-2 comprised the reference trace, and the immediately subsequent experiment (in this case Post-3#1) formed the traces to be aligned. The traces to be aligned had the same source and receiver locations as the previous experiment, to the best of the field crew's ability to reoccupy the locations. Instead of aligning the EMP pulses, the time lag between the first-arrivals of the two experiments was found. The Post-3#1 travel-time pick was then calculated by adding the positive or negative cross-correlation lag at the maximum normalized cross-correlation coefficient. Arrival-time picking for subsequent experiments followed this same pattern. For example, Post3#1 was used as the reference event for Post-3#2, and so on.

Because of waveform differences among the experiments (due to explosion size, rays traversing newly damaged rock, small misalignment of source or receiver location, etc.), we empirically determined the filter bands and time-window lengths that resulted in the most accurate cross-correlations. Twelve different filter bands and time windows (centered on the first arrival) were examined, stepping through a grid-search algorithm. The time lag at maximum CCC of this set was used unless the CCC was less than 0.75, in which case it was discarded.

5. RESULTS

5.1. Cross Correlations

Fig. 6 shows the results of the max CCC found using our method. The x- and y-axes represent the depth, in meters, of the source and receiver in BH-189 and BH-009, respectively. We assume source–receiver reciprocity, i.e. we make no distinction if the sparker was swapped for geophones, or vice versa, in a borehole. After the first cross-correlation change detection experiment (Post-2 to Post-3#1), Fig. 6 has two tracks. The top track (Figs. 6e, f, and g) show CCC relative to the Post-2 Baseline experiment, while the bottom track (Figs. 6b, c, and d) show CCC relative to the survey immediately prior.

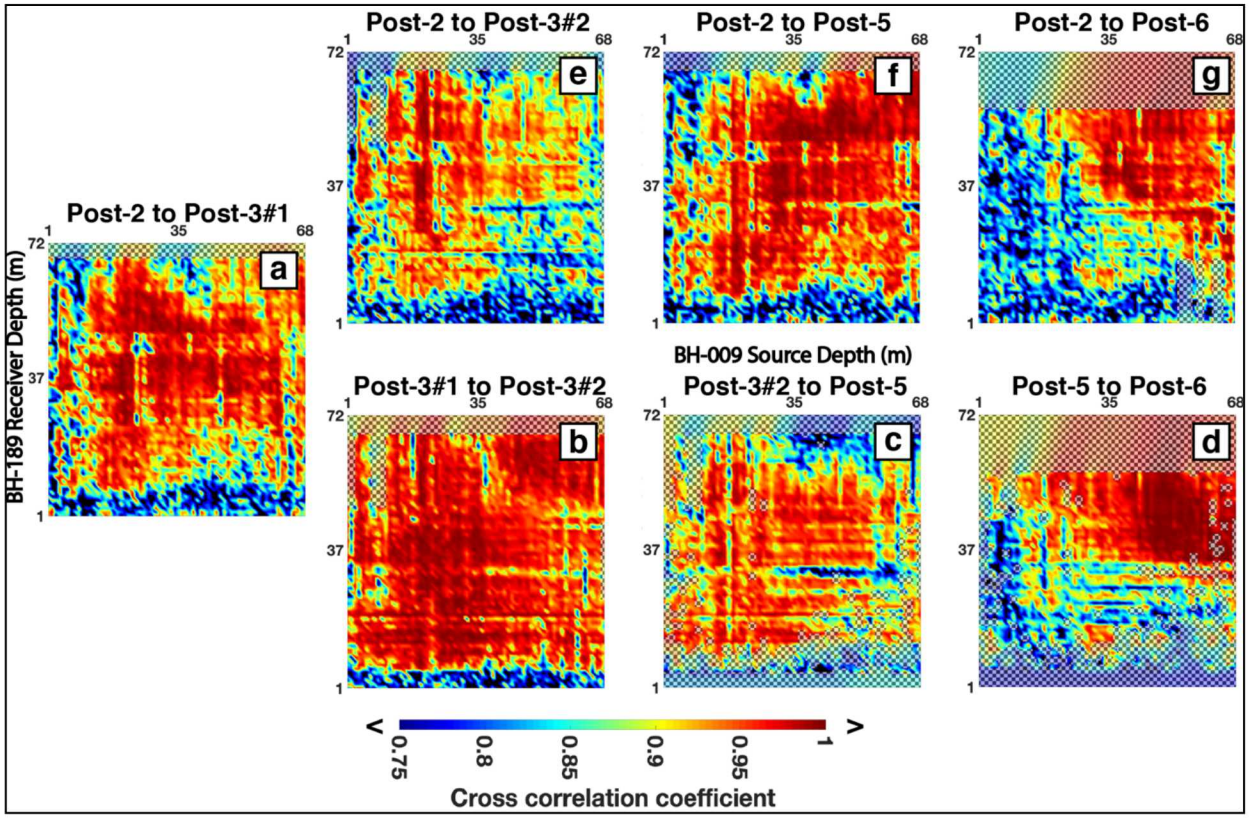

Figure 6. Normalized cross-correlation coefficient matrices. Vertical axis is BH-189 and horizontal is BH-009. Checkerboard patterns overlay data locations that were not sampled in both surveys.

- CCC for very shallow (< 5 m) raypaths are generally the lowest for any survey. We attribute this to the attenuation and scattering the seismic waves occurring in the weathered zone near the surface. This can be seen near the bottom and left hand-axes on each subfigure.
- In general, CCC is lower where there is a large mismatch in receiver depth (i.e., shallow in one hole and deep in the other). This can be related to the length of the raypaths in the shallow subsurface, as well as to the fact that these raypaths are the longest in the dataset.
- CCC, on average, is lower among successive experiments as the SPE explosion series progressed. For instance, the average CCC for Post-5 to Post-6 is less than Post-3#2 to Post-5 which was less than Post-2 to Post-3#1 (Figs. 6b, c, and d). Our interpretation is that, as the geologic media gets more and more damaged by the explosions, the waveforms become increasingly dissimilar due to scattering, multi-pathing, and attenuation.

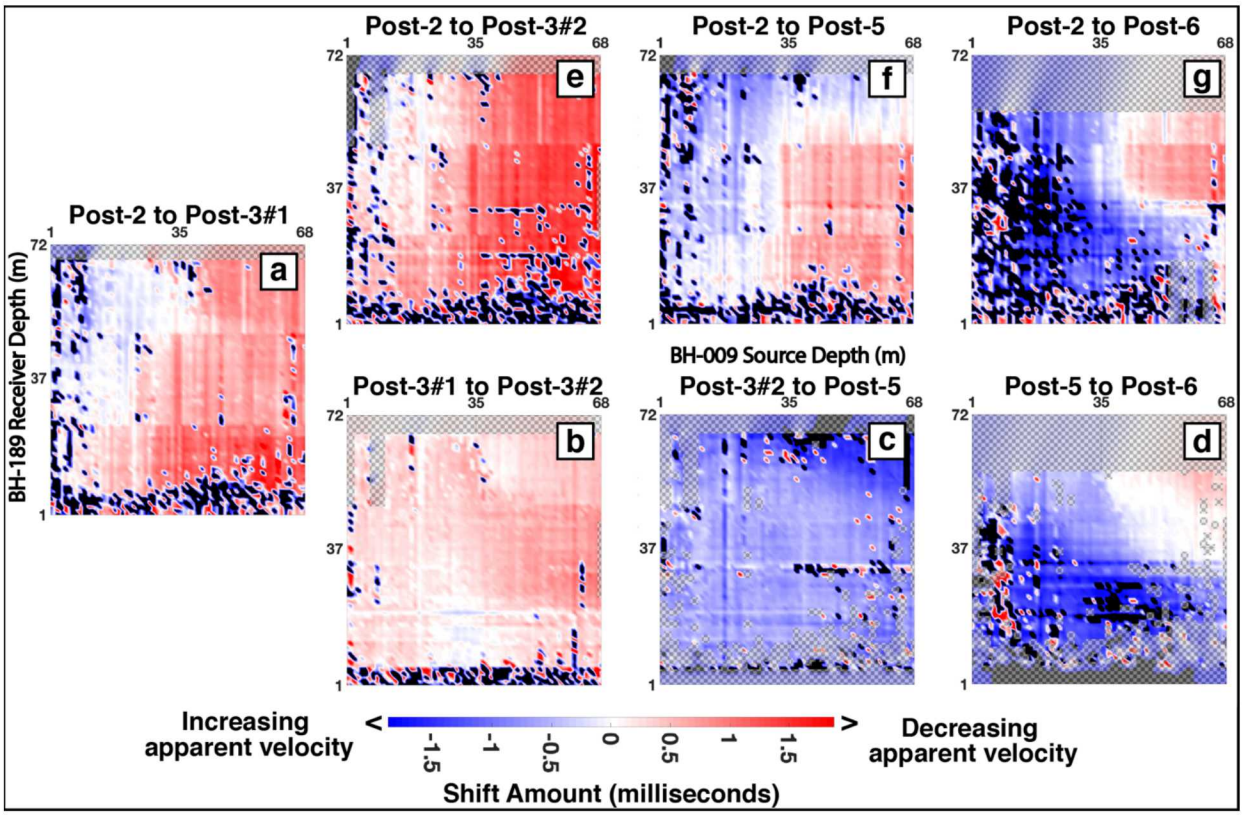

Figure 7. Time lag at maximum normalized cross-correlation coefficient matrices. Vertical axis is BH-189 and horizontal is BH-009. Checkerboard patterns overlay data locations that were not sampled in both surveys.

5.2. Time Lags

Similar to Fig. 6, Fig. 7 shows the computed time lags associated with the maximum CCC. Colder colors represent negative time lags (decreases travel time and therefore faster velocity), and warmer colors represent positive time lags (slower velocity).

- The biggest increase in time lags occurred for the Post-2 to Post-3#1 experiment.
- Post-3#1 to Post-3#2 had the least amount of change. This was to be expected because no explosions occurred between the two experiments.
- After Post-3#1 to Post-3#2, the general trend was towards negative time lags (increasing velocity). This is despite the supposed increased damage of SPE-4 prime, SPE-5, and SPE-6 explosions. This will be discussed more in the DISCUSSION section.

5.3. Velocity Tomography

The data were inverted using *Tomog*, an internal Sandia National Laboratories tomography code that exploits a ray-based (eikonal) P-wave travel-time tomographic inversion methodology (Preston, 2009). Input P-wave travel times are weighted by estimated error, and uniform error is assumed (i.e., equal weighting on all observations). Model parameters are continuously evaluated up to a pre-defined set of convergence criteria through an iterative inverse procedure using incremental changes

in model parameters based on travel-time residuals (i.e., observed minus calculated). After model convergence criteria are met, the final P-wave tomogram is produced.

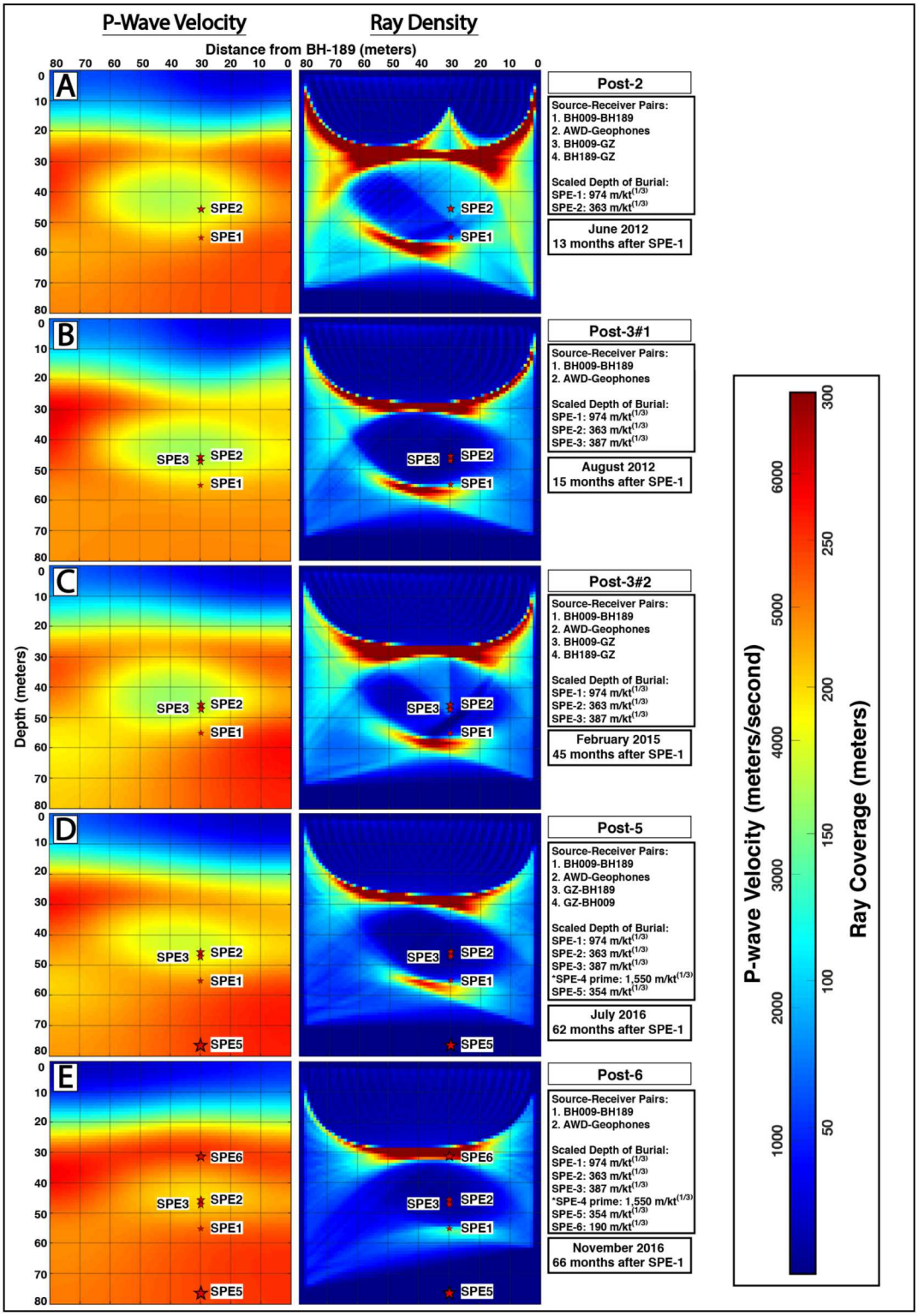

Figure 8. (left) P-wave velocity tomograms, (middle) P-wave raypath density, and (right) Survey acquisition parameters for (A) Post-2, (B) Post3#1, (C) Post3#2, (D) Post-5, and (E) Post-6 surveys.

5.3.1. Velocity Gradient Effects

The velocity anomaly in our models show a significant absence of raypath coverage at its center. This suggests that first-arriving waves avoid low velocities in this region. (e.g. Fig. 8). Predominantly horizontal raypaths deeper than the surface-surface raypaths distort model structure at depth. Using the source-receiver geometry of Post-6 (Fig. 8), Fig. 9 demonstrates a forward model of a perfect low-velocity circle (Fig. 9.A) (-400 $m \bullet s^{-1} \bullet m^{-1}$) yields an ellipse in the reconstructed velocity model.

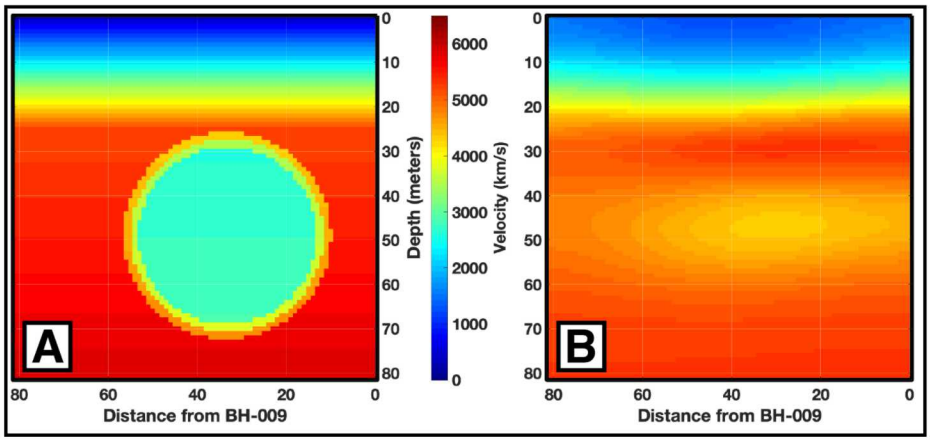

Figure 9. A) Example of forward modelling a circular negative velocity gradient. B) P-wave inversion that used the calculated pick times from the forward model. Data coverage used in this forward model is identical to the post-6 survey (Figure 8).

5.3.2. Before SPE-1 and SPE-2

Since the boreholes used for the cross-borehole seismic studies were not drilled until after the SPE-2 experiment, neither SPE-1 (55 m DOB, 90 kg TNT-equivalent yield) nor SPE-2 (45.7 m DOB and 997 kg yield) had downhole surveys before their detonation. We must rely upon the pre-drilling site survey to determine a baseline. As mentioned previously, the results suggest a 25 m thick weathered zone over a half-space. There was no indication of a low-velocity zone near GZ below the 25 m depth (Fig. 3).

5.3.3. Post-2 Baseline Survey

The Post-2 Baseline survey established the velocity tomogram to which the Post-3#1 Change Detection Survey was to be compared. The survey was taken after SPE-2 (45.7 m DOB and 997 kg yield). The general trend of velocity increasing with depth that we saw in the surface survey is also seen in these results (Fig. 8a). Immediately apparent in the tomogram is a striking, ellipsoidal low-velocity zone near the SPE-2 detonation point. This was not seen in the surface-only survey and is a result of the SPE-2 (and perhaps SPE-1) explosion (Fig. 10). The change in velocity near the center of the ellipsoid relative to surrounding media is about 20%. The ellipsoid is wider than it is tall as a consequence of poorer resolution laterally, as most of the raypaths are horizontal once they are below the penetration depth of the AWD survey (approximately 25 m). Although the ellipsoid is not centered on SPE-2, there is evidence that the damage seen on the surface by other techniques is not centered over GZ, as well. Both photogrammetry (Schultz-Fellenz et al., 2018) and surface crack mapping (Gang et al., 2016) indicate increased damage to the northeast, as in our results.

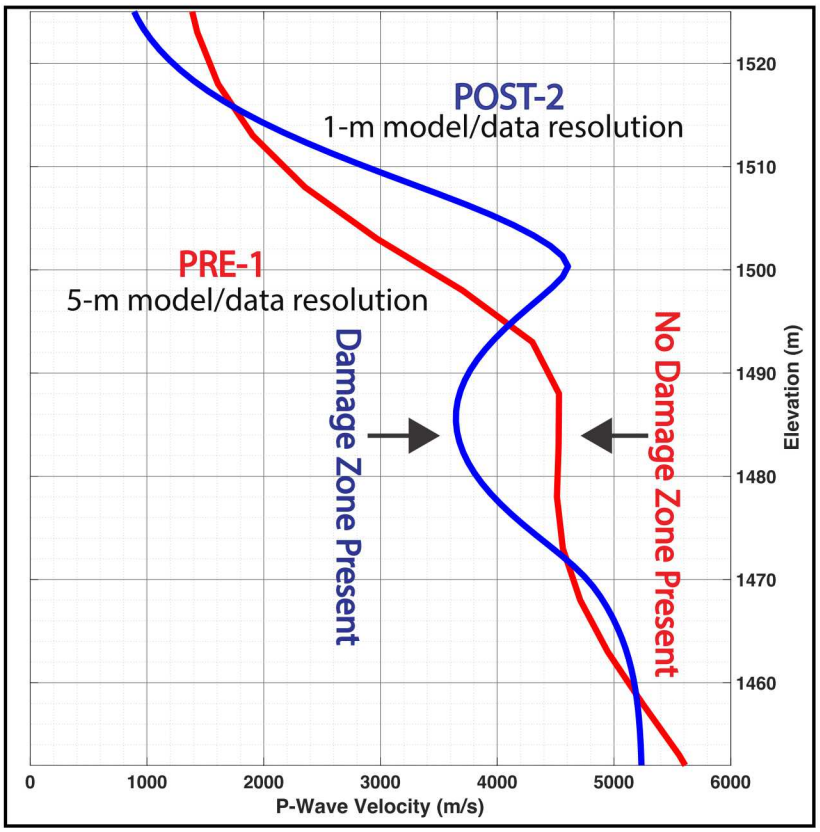

Figure 10. 1-D P-wave velocity tomograms for Pre-1 and Post-2 surveys.

5.3.4. Post-3#1 Change Detection Survey

The first explosion for which we could complete a true before-and-after change detection survey was SPE-3 (47.2 DOB and 905-kg TNT-equivalent). SPE-3 was designed as a twin to SPE-2 (45.7-m DOB and 997-kg TNT equivalent) in both yield and depth. The goal was to compare the seismo-acoustic recordings from SPE-2 and SPE-3 to determine if detonating SPE-3 in the damage zone of SPE-2 would have an effect.

The Post-3#1 tomogram (Fig. 8b) is remarkably similar to that of Post-2. The ellipsoidal low-velocity zone is still present. The velocity is slightly lower, consistent with increased damage, and the ellipsis is slightly more elongated horizontally. The elongation may be due to not having receivers in the GZ hole, unlike for Post-2. These central GZ raypaths, going to both perimeter boreholes, would have the effect of better localizing the anomaly.

5.3.5. Post-3#2 Change Detection Survey

Unlike previous surveys, the Post-3#2 Change Detection Survey did not take place after an intervening explosion. There were two reasons for this. Firstly, the SPE-4 explosion was scheduled to have only 100 kg yield, and it was to be below the depth of the perimeter boreholes. We determined that we would likely see no effects from damage under those conditions and did not schedule a "Post-4" survey. When the SPE-4 experiment failed to detonate, however, an unusually large time gap was opened between Post-3#1 and the next scheduled data collect, Post-5 (51 months). We decided that a second Post-3 survey, partially filling the time gap, would be useful to determine 1) the repeatability of the surveys when no large changes are expected, and 2) track any damage "healing" effects over time.

With the ability to reoccupy GZ with receivers, the Post-3#1 damage ellipsoid (Fig. 8c) resolved as more horizontally compact again, more closely resembling Post-2. There were no other large changes relative to Post-3#1, though perhaps a very small decrease in velocity overall (as can be seen in the time lag matrix, Fig. 7b).

5.3.6. 5.4.5. Post-5 Change Detection Survey

SPE-5 (76.5 m DOB and 5,035 kg yield) was the largest and deepest explosion in the SPE series. It was, however, at the very edge of our model, where raypath density is extremely low (Fig. 8d). As such, damage at the detonation point was not resolvable. The effect of SPE-5 on the overlying material was expected to be that of decreasing P-wave velocity, but it instead showed increasing velocity. In essence, seismic ground motion from SPE-5 seemed to heal damage from the previous explosions. This is an unexpected result. This result will be examined more in the DISCUSSION section.

5.3.7. 5.4.6. Post-6 Change Detection Survey

SPE-6 (31.4 m DOB, 2245 kg yield) was the shallowest of the explosions and still of considerable yield. Given that SPE-6, unlike SPE-5, was at a depth for which we have robust raypath coverage, we expected to see a damage zone similar, or greater in magnitude, to that for SPE-2. In actuality, the Post-6 tomogram reveals no discernible damaged area at the SPE-6 depth (Fig. 8d). In addition, we saw a decrease in the velocity anomaly from SPE-2/3. Again, we see that a large explosion tended to heal damage from a previously detonated one.

6. DISCUSSION

The novel result of this study is the conclusion that explosions in intact rock can produce extended damage zones, but subsequent explosions in the damaged media either do not produce more damage, or they tend to heal the initial damage. SPE-2, as seen in the Pre-1 and Post-2 surveys, resulted in an extended zone of low seismic P-wave velocity at and above the detonation location (Figs. 8a and 9). The velocity was reduced on the order of 20% relative to adjacent media at the same depth. Following SPE-5, the Post-5 tomogram (Fig. 8d) shows increased P-wave velocity within the SPE-2/3 damage zone. The Post-6 tomogram (Fig. 8e) furthers this trend in the SPE-2/3 damage zone. Furthermore, there was no discernible change in the P-wave velocity at the SPE-6 depth, despite ample raypath coverage in the vicinity of the explosion (Fig. 8e).

We propose, as a possible explanation for these apparently contradictory results:

- If detonated in intact rock, the gasses produced by the explosion have no way to dissipate. The increased gas pressure results in fracturing the rock to create porosity. As the gas migrates into the newly created fractures, the fractures increase in size and distribution. This fracturing reduces the seismic velocity, as seen in the tomograms.

- Subsequent explosions, now taking place in a pre-fractured medium, have plenty of avenues for the gas to escape. Therefore, the need to damage the medium for pressure relief is greatly reduced. This results in damage that is difficult to see with the seismic cross-borehole method, or is in fact, not present at all. Under this hypothesis, SPE-5 should have produced a damage zone at 75 m depth, but our borehole geometry meant we had insufficiently deep sources and receivers to have adequate raypath coverage to resolve it.

- SPE-6, detonated within 15 m depth of SPE-2/3, was able to propagate through the fracture network of the previous explosions without any new discernible fracturing.

The SPE-2/3 damage zone appears to heal after subsequent explosions in the SPE series. At first glance, it would seem that the intervening months and years between shots is related. Indeed, one could see a mechanism where water flows though the fractures and deposits sand, silt, etc., in the fractures and in effect closes them. Water flowing through the fractures could be precipitating minerals, as well. In addition, the effect of overburden pressure constantly pressing the fractures closed might be at work. Healing of fractures appears to be apparent between Post3-#2 and Post-5 (47 months duration) and Post-5 and Post-6 (4 months duration).

There appears to be as much healing in the four months between Post-5 and Post-6 as in the almost four years between Post-3#2 and Post-5. This, and the fact that between Post-3#1 and Post-3#2 (30 months duration) no healing at all was seen in the time lags (Fig. 6) or the tomograms (Fig. 8). This would argue for the hypothesis that the healing was a nonlinear (temporally) process that accelerates with time. SPE-5 (deeper) and SPE-6 (shallower) both produced large amplitude waves that traversed the damage zone from SPE-2/3. Perhaps this transient pulse of seismic waves compacted and closed favorably-oriented fractures from the previous detonations. This hypothesis would fit the data better in that no healing was observed when no detonation occurred despite 30 months of intervening time. Also, the most healing was observed after SPE-6, which, while being smaller in size than SPE-5, was less than half the distance to the fractured rock mass of the SPE-2/3 damage zone.

7. CONCLUSIONS

We acquired and analyzed surface and cross-bore seismic data in the vicinity of a series of large chemical explosions on the NNSS. Whereas a pre-explosion dataset showed a relatively simple increase of seismic P-wave velocity with depth, post-explosion datasets revealed an extended region of lower velocity. We interpret decreased velocity as resulting from fracturing of the previously intact geology by the explosions. The cumulative effect of multiple subsequent explosions did not produce the expected result of velocity reduction. Instead, hypocenters of later explosions (SPE-5 and SPE-6) were not associated with damage zones whether due to lack of ray coverage (SPE-5) or the hypothesized stress-relieving properties of detonating near existing fracture zones (SPE-6). In addition, the SPE-2/3 damage zone appeared to heal from June 2012 to November 2016. This could be due to either a slow (but accelerating) process of fracture sedimentation, mineralization, and compaction, or due to the compression of seismic-wave pulses from SPE-5 and SPE-6.

REFERENCES

Houston, L. M. (1992). Tube wave suppression: A comparison of median filtering and nearest-neighbor subtraction approaches. In SEG Technical Program Expanded Abstracts (pp. 128–132).

Gang, H., Drellack, S., Reed, D., and J. Mercadante (2016). Geologic Surface Effects Mapped Following Source Physics Experiment 5 (SPE-5), *National Security Technologies Report*, 79 p.

Patton, H. J. (1988). Source models of the Harzer explosion from regional observations of fundamental-mode and higher mode surface waves. *Bulletin of the Seismological Society of America*, *78*(3), 1133-1157.

Preston, L. (2009). Tomog User Manual Technical Paper, SAND2009-3082P, Sandia National Laboratories, Albuquerque, NM, 21 p.

Schultz-Fellenz, E. S., Coppersmith, R. T., Sussman, A. J., Swanson, E. M., & Cooley, J. A. (2018). Detecting Surface Changes from an Underground Explosion in Granite Using Unmanned Aerial System Photogrammetry. *Pure and Applied Geophysics*, *175*(9), 3159–3177.

Snelson, C. M., Abbott, R. E., Broome, S. T., Mellors, R. J., Patton, H. J., Sussman, A. J., Walter, W. R. (2013). Chemical explosion experiments to improve nuclear test monitoring. *Eos, Transactions American Geophysical Union*, *94*(27), 237-239.

Taylor, S. R., & Randall, G. E. (1989). The effects of spall on regional seismograms. *Geophysical Research Letters*, *16*(2), 211-214.

Townsend, M., Prothro, .L, and C. Obi (2012). Geology of the Source Physics Experiment Site, Climax Stock, Nevada National Security Site, *Technical Report DOE/NV/25946--1448*, National Security Technologies, LLC, Las Vegas, Nevada, 442 p.

DISTRIBUTION

Email—Internal

Name	Org.	Sandia Email Address
Technical Library	01977	sanddocs@sandia.gov

This page left blank

Sandia National Laboratories

Sandia National Laboratories is a multimission laboratory managed and operated by National Technology & Engineering Solutions of Sandia LLC, a wholly owned subsidiary of Honeywell International Inc. for the U.S. Department of Energy's National Nuclear Security Administration under contract DE-NA0003525.